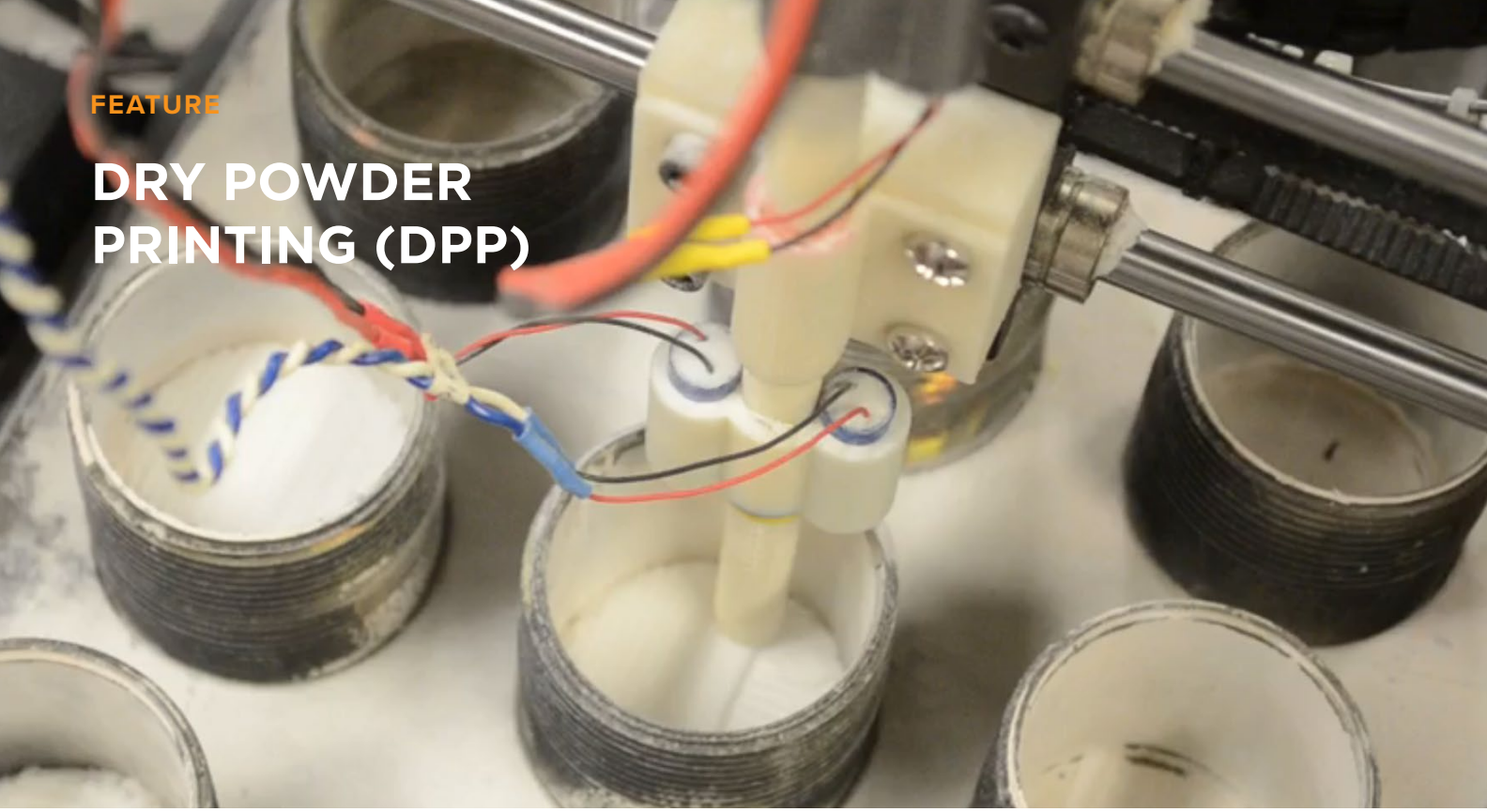

FEATURE

DRY POWDER PRINTING (DPP)

Tailorable Energy Absorbing Cellular Materials via Sintering of Dry Powder Printed Hollow Glass Microspheres

Norman Wereley[1], Jungjin Park[1], John Howard[2], Matthew DeMay[2], and Avi Edery[2]

[1]Composites Research Laboratory, Department of Aerospace Engineering, University of Maryland, College Park, MD USA

[2]Microsphere Material Solutions, Rockville, MD USA

Email: wereley@umd.edu

ABSTRACT

This article examines amorphous glass-based foams as lightweight core materials for crash-resistant structures that offer tailorable energy absorption capabilities. Hollow glass microspheres (HGMs) of different densities are layered using dry powder printing (DPP), an additive manufacturing process, and subsequently sintered to consolidate these microspheres into a cellular foam structure. The tailoring of energy absorption is achieved in these foams by layering hollow microspheres with different densities and different thickness ratios of the layers. The mechanical response to quasi-static uniaxial compression of the bilayer foams is also investigated. Bilayer samples exhibit a distinctive two-step stress-strain profile that includes first and second plateau stress, as opposed to a single constant density which does not. The strain at which the second plateau occurs can be tailored by adjusting the thickness ratio of the two layers. The resulting stress-strain profiles demonstrate tailorable energy absorption. Tailorability is found to be more significant if the density values of each layer differ greatly. For comparison, bilayer samples are fabricated using epoxy at the interface instead of the co-sintering process. Epoxy-bonded samples show a different mechanical response from the co-sintered sample with a different stress-strain profile. Designing the bilayer foams enables tailoring of the stress-strain profile, so that energy-absorption requirements can be met for a specific impact condition. The implementation of these materials for energy absorption, crashworthiness, and buoyancy applications will be discussed.

DOI: 10.33599/SJ.v60no3.04

1. INTRODUCTION

Foams also known as cellular solids are currently used in various applications, including crash-worthiness applications, from occupant protection systems in automobiles or aircraft to electronic packaging[1,2,3], armor[4,5,6], load-bearing structures[7,8], buoyancy[2,9,10], and thermal insulation[11,12,13,14], noise insulation[15,16,17], and catalytic processes[18,19]. Foams are used widely for energy absorption because foams undergo large strain deformation at relatively constant stress. Energy absorption occurs through compression of microcellular structures under large strain, making foams suitable for use in automotive bumpers, personal protective gear, and armor for shock wave attenuation and impact energy dissipation[20,3,21,22,23,24]. Since the primary contribution to the energy absorption capacity of the foams comes from the specific strength of the bulk material and its densification strain, materials with high specific strength are desired to develop cellular solids with superior energy absorption capacity. Research performed by Wiest et al., identified silicate glasses as the potential material candidates with their much higher specific strength in comparison to that of steels, bulk metallic glasses (BMGs), titanium, and aluminum alloys[25,26]. The achievement of making foams with glass material has been realized using hollow glass microspheres (HGMs). They are commonly used in syntactic foam, which is a polymeric matrix filled with hollow microspheres[27,28,29]. Recently, glass materials have been used to form cellular structures by sintering hollow glass spheres together[25,30,31,26,32,33]. This method does not require the use of binding agents or blowing agents and can be used to fabricate both open- and closed-cell foams. Various types of feedstock materials are commercially available, and the mechanical properties of glass foams can be related to the mechanical properties of the feedstock. Unlike syntactic foam, the glass foam manufacturing process usually does not require matrix resin or other chemical additives[34,35,36]. Glass foam is a homogeneous system, so that glass foam can achieve thermal stability up to 600°C, which usually cannot be achieved with syntactic foam due to polymeric binders or matrices. Consequently, the adequate heat resistance of the glass material could serve as an advantageous factor for applications utilized in high-temperature environments.

Glass foam manufacturing will impact various commercial sectors, each with unique considerations (Figure 1). Low-density, high-strength glass foam holds potential in the market for buoyancy in submersible vehicles. The growing trend for smaller autonomous underwater vehicles (AUVs) and micro-unmanned underwater vehicles (UUVs) underscores the importance of buoyancy materials[37]. Combining glass foam with lightweight armoring materials could lead to lighter armor with an increased ballistic rating[38]. In the automobile industry, where safety regulations continually evolve, the lightweight foam could reinforce vehicle frames and improve occupant safety in collisions[39]. Furthermore, filling empty spaces with innovative

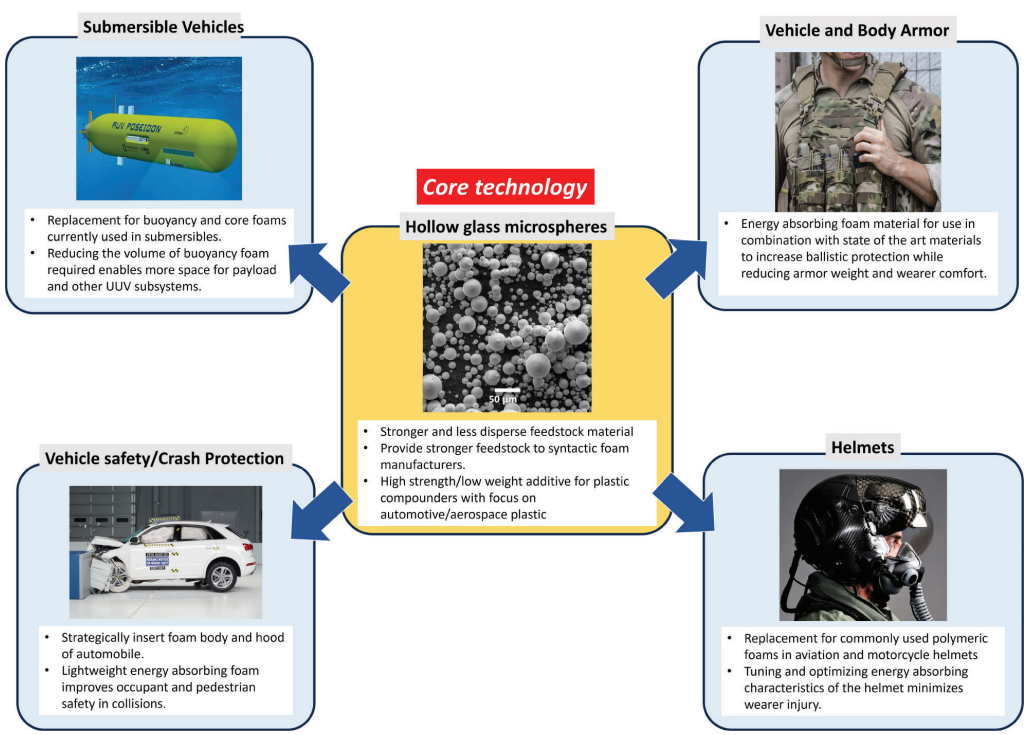

Figure 1. Hollow glass microspheres in foams have applications to buoyancy, armor, and occupant protection domains.

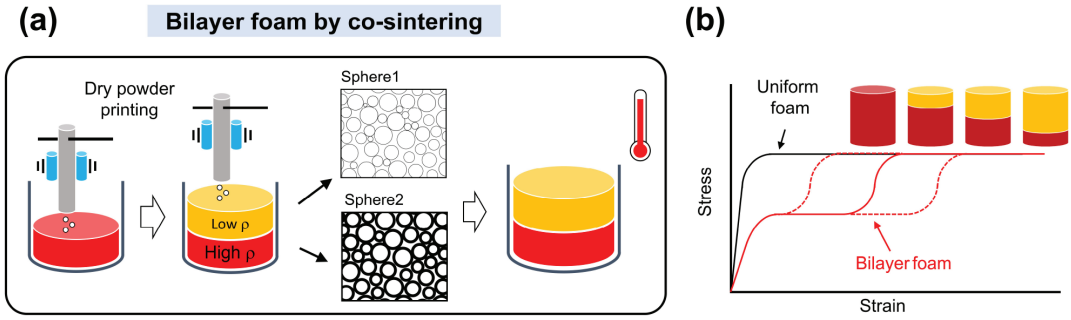

Figure 2. (a) Schematic of the co-sintering process used to produce multilayer cellular foam using hollow spheres of different densities in each layer. b) Qualitative depiction of the stress–strain characteristics of uniform (black)and bilayer foams (red). The dashed red curves represent the tailored load vs. stroke profile obtained for different layer thicknesses.

foam could tailor the crush rate of vehicle zones, significantly reducing the acceleration pulse felt by occupants without adding significant weight. This reduction in vehicle weight could lead to increased fuel efficiency. Furthermore, glass foam could be used in prototype bicycle and motorcycle helmets, replacing traditional foam materials. While maintaining the outer shell and soft inner materials, glass foam would offer enhanced energy absorption capabilities. The majority of applications focus on the energy-absorbing capabilities of glass foam.

Recently, research into tailorable energy absorption has been undertaken to enhance the capabilities of glass foam. The advancement of crashworthiness applications, spanning from occupant protection systems in automobiles or aircrafts to electronic packaging, could greatly benefit from a material system with tailorable energy absorption. Such a system would gradually increase the stroking load, thus reducing the acceleration and peak stress encountered[1,3,2]. For instance, adaptable passenger seats could be engineered for passengers with varying weights, effectively absorbing transmitted stress through an energy-absorbing layer tailored for occupant weight[40]. Multiple research studies have shown that graded cellular structures allow for gradual collapse, resulting in enhanced energy absorption, which is advantageous for shielding payloads from dynamic loads[41,42,43]. Graded porous structures and syntactic foams are typically manufactured by either bonding multiple layers or introducing blowing agents. More recently, sintered glass foam with density gradients has demonstrated progressive structural collapse during crushing, illustrating its energy absorption tailorability[30,44]. These studies showcased the potential tailorability of glass foam by creating a bilayer structure, which effectively regulates the shape of stress-strain curves to some extent.

In our lab, a dry powder printing (DPP) system was developed in order to manufacture a layered structure, enabling the fabrication of bilayer foam samples with precise control over layer thickness and ensuring a consistent uniform interface between the layers. This system successfully achieved a consistent printing rate and uniform spatial printing. The bilayer structures are produced by printing two types of spheres with different densities, and the resulting powder compacts are sintered in a furnace (Figure 2). Consequently, incorporating different densities in a bilayer sample allowed for the adjustment of the stress-strain curve. This adjustment was achieved by sequentially compressing the lower-density layer followed by the higher-density layer. As depicted in the Figure 2, the stress-strain characteristics of uniform (black) and bilayer foams (red) are qualitatively illustrated. The thickness ratio between the low and high-density foam layers could be varied to represent a tailored loading profile. Three configurations of thickness ratios between layers were utilized. The sintered bilayer foam exhibited a sequential collapse of its constituent layers, resulting in a step-like progression in the stress-strain profile. Furthermore, the onset strain for the second plateau stress could be controlled by adjusting the thickness ratio of the layers.

This paper will discuss the utilization of hollow glass spheres within highly porous glass foam, the development of dry powder printing technology, and the exploration of its tailorable energy absorption properties.

2. DRY POWDER PRINTING

Conventional methods of fabricating gradient foam structures often involve gluing together multiple foam layers, which can lead to high peak stress at the interface. Conversely, multi- layered glass foams can be sintered simultaneously (co-sintering), resulting in a smoother density transition at the interface. This interface facilitates a gradual energy absorption through sequential collapse, reducing peak stress during impact. To achieve this layered structure, a dry powder printing (DPP) system was developed (Figure 3). This system enables the fabrication of bilayer foams with precise control over layer thickness and ensures a uniform interface between the two layers.

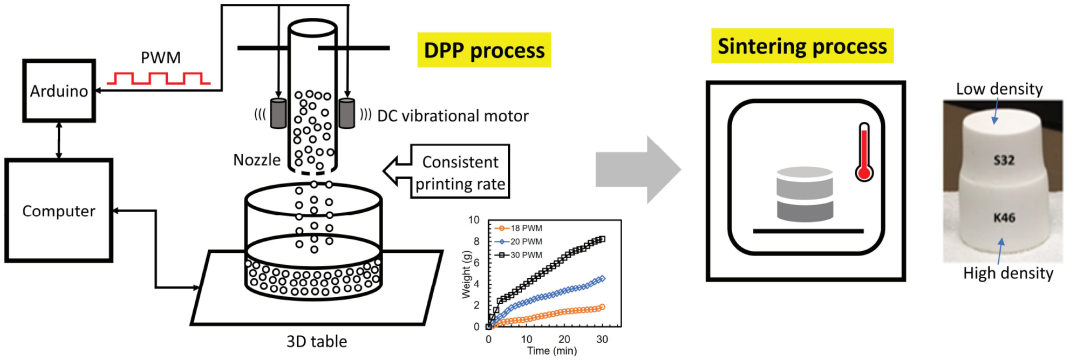

Figure 3. Scheme of the experimental setup for dry powder printing (DPP) and sintering process.

Various powder delivery systems have been developed, with acoustics and ultrasonication being popular methods for controlling powder dispensing[45,46,47,48]. While many approaches utilize tapered pipette-type nozzles for patterning with controlled lateral resolution, our application necessitates the use of a cylinder with multiple nozzles because tapered nozzles cannot effectively print powder around the edge of the mold, which lead to non-uniform powder distribution as HGMs were not printed evenly across the entire surface. As a result, the nozzle of our DPP system was specifically engineered to fulfill this requirement, featuring a diameter of 10 mm and equipped with 15 small holes, each measuring 1 mm in diameter, to accurately dispense HGMs.

To address this, a motor-driven vibratory method with low frequency was chosen. The powder flow needs to be controlled to stop printing once a layer is complete. Vibration may also be used to increase the free volume in a powder and allow a static powder to flow. Vibration is also known to increase the packing efficiency of granular materials[49]. In addition, a wide particle size distribution of the HGMs aids in efficient packing. After the optimized vibrational amplitude and frequency are determined, it is employed to regulate both the initiation and cessation of powder flow, as well as to modulate the flow rate. Consequently, it has the characteristics of both a proportioning valve, regulating the flow rate, and an on/off valve, controlling the initiation and cessation of flow.

A consistent printing rate and uniform spatial printing were achieved by modifying a commercially available 3D printer to implement the DPP system (Figures 3 & 4). The extruding system was replaced with a custom dry powder dispensing nozzle equipped with small holes for dispensing HGMs. Two DC vibrational motors were attached to the nozzle to control actuation via Arduino and actuation was controlled by adjusting pulse width modulation (PWM). Optimization of powder printing parameters, such as feeding rate, infill rate, infill pattern, and layer height, was conducted. Testing revealed that a PWM value of at least 20 is required to dispense spheres effectively.

3. OPTIMIZATION OF GLASS FOAM SINTERING

Sintering process optimization is critical to achieving high energy absorption while maintaining a low foam density. Figure 5 illustrates an instance of the optimization process. Foam samples are formed from HGMs consolidated above the glass transition temperature (T_g). These spheres come in contact with adjacent spheres when compacted. When the consolidated spheres are raised above their T_g, they begin to soften and flow in a viscous manner, leading to bonding between adjacent spheres. The energy absorption of the resulting glass foams, which is the area under the stress-strain curve, is maximized by choosing a feedstock material with high specific strength. Also, a wide variety of HGMs are readily available with different cell sizes, densities, and strengths,

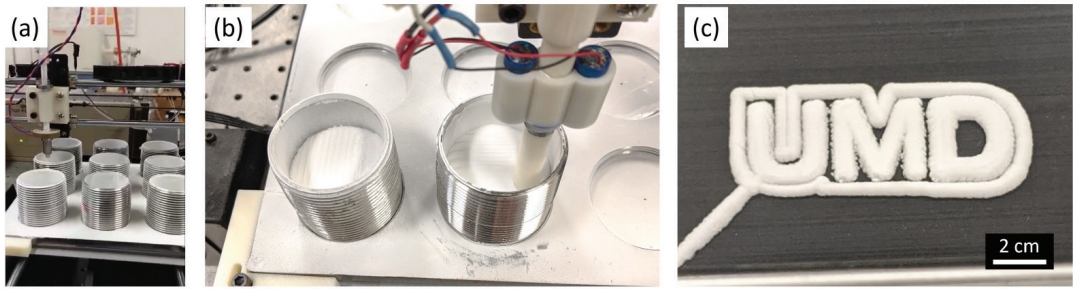

Figure 4. (a) DPP set up (b) image of dry printing process (c) dry printed HGMs into letter UMD.

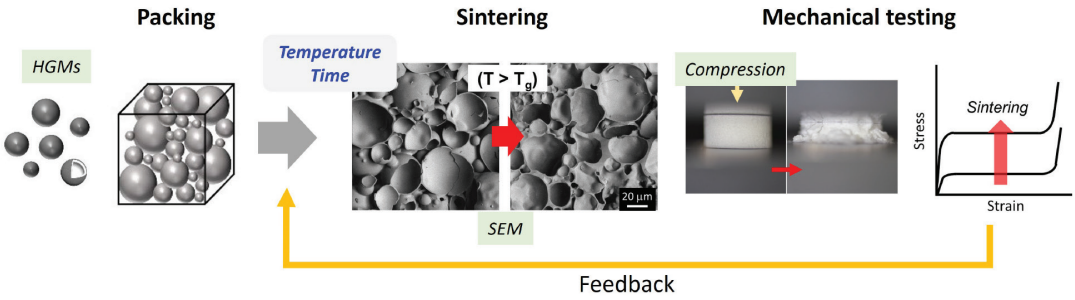

Figure 5. Conceptual figure of glass foam process optimization.

providing a means to uniquely tailor the mechanical behavior of the cellular structure. Therefore, the density, strength, and stiffness of glass foams can be tailored within feasible ranges to meet the requirements of a particular application.

The effects of sintering temperature and duration on the microstructural evolution and resulting energy absorption capacity of glass foam can be optimized as a feedback process. Scanning electron microscope (SEM) observation reveals how thermally induced consolidation evolves between microspheres for different processing parameters, such as the sintering temperature and duration. SEM observation in conjunction with uniaxial compression tests enables a more accurate determination of the processing conditions possible.

3.1 Process Optimization

An example of process optimization is summarized in Figure 6. Various samples were generated across a spectrum of sintering temperatures ranging from 760 to 860°C, and their resultant microstructures were observed using SEM. The micrograph depicts the persistence of the spherical shape of glass spheres, alongside localized densification at the cell walls of these spheres starting at 760°C. Due to the considerable dispersion in sphere diameters, there's an opportunity to arrange smaller spheres within the gaps of larger ones, such as octahedral and tetrahedral interstices, thereby enhancing packing density. With an increase in sintering temperature, the microstructure manifests enhanced local consolidation through bonding between adjacent glass spheres. Initially, the microstructure predominantly exhibits a closed-cell configuration until it reaches 800°C. Beyond this temperature, significant deformation occurs, accompanied by the emergence of open voids as spheres continue to consolidate. At 840°C, as spheres undergo consolidation, the struts thicken and interconnect more prominently. Subsequently, at temperatures exceeding 840°C, larger open voids become apparent, exemplified in the 860°C sample. The presence of cracks larger than 1 µm correlates with decreased fracture strength. Identifying open voids exceeding 20 µm in length in foams consolidated above 840°C indicates a potential risk of brittle fracture under low-stress conditions.

Quasi-static compression measurements, coupled with SEM analysis, determined the optimal processing conditions. By controlling sintering temperatures and duration, the microstructure of glass foams can be effectively consolidated, leading to a maximum energy absorption capacity of approximately 5 MJ/m^3 (Figure 6). Results indicate that bonding at 810–840°C for 30 minutes optimizes foam consolidation, yielding the highest energy-absorbing properties. Other processing parameters like ramp rate, cooling rate, and annealing temperature are also crucial, particularly for larger sample sizes, as temperature gradients across larger samples can significantly impact results.

3.2 Deformation-Mechanism Map

Optimization of process parameters leads to specific energy absorption performance of a glass foam material, which will be presented as a deformation-mechanism map. When a foam undergoes compression, it initially experiences linear-elastic deformation, followed by plastic collapse. Eventually, the cells collapse completely, causing a rapid increase in stress as the opposing cell walls are pressed together. It is practical to represent the dominance of each deformation phase through a map featuring axes of normalized compressive stress and compressive strain. The mechanical properties of glass foams can vary depending on their density, which can be controlled by selecting appropriate feedstock materials. Therefore, the relative density of foam samples is utilized to construct a deformation map. This visualization in Figure 7 illustrates the domains in which each mechanism is dominant. When a foam is compressed,

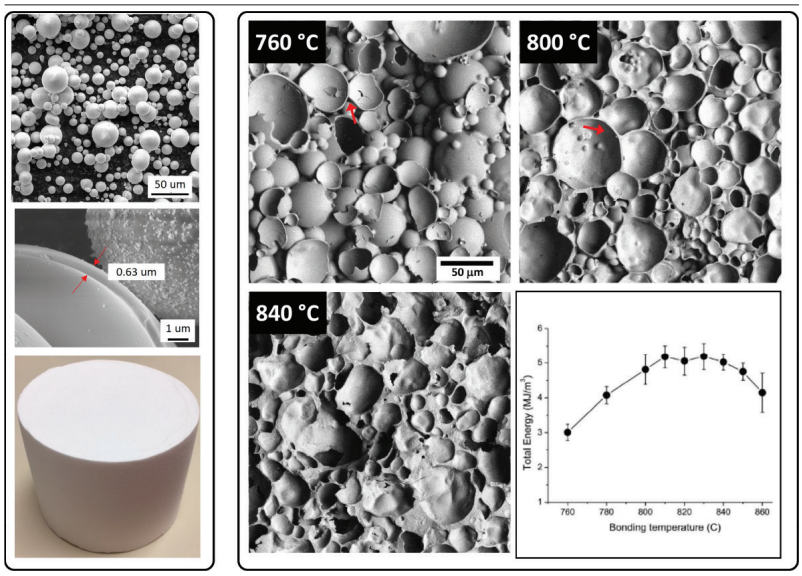

Figure 6. (Left) SEM micrograph of hollow glass microspheres (HGM) and wall thickness of HGMs. Photograph of a sintered 4-inch diameter glass foam. (Right) SEM micrographs of the glass foam microstructures for different temperatures and total energy calculated from compression testing as a function of sintering temperature.

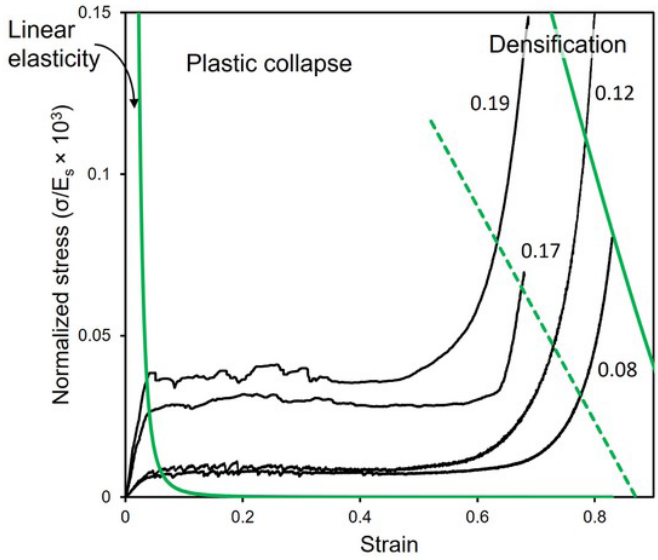

Figure 7. A deformation-mechanism map is developed for uniform glass foams. Each foam possesses relative densities of 0.08 through 0.19. In the map, a heavy green line delineates the field boundary, while dotted line indicates empirical boundaries.

it first deforms in a linear-elastic way. The boundary of the linear-elastic field (green line) is obtained from

$$\frac{\sigma}{E_s} = (0.65\frac{\sigma_y}{E_s})^4 \frac{1}{\epsilon^3} \qquad [1]$$

σ_y is the yield strength of cell-wall material and E_S is the Young's modulus of cell-wall material. The equation was obtained from the equations related to linear elasticity and plastic collapse[50]. When building this map, it was assumed that σ_y/E_S =0.01. Adjacent to the linear-elastic field lies the field of plastic collapse. With brittle glass foams, progressive crushing can again lead to a plateau, ending when the material is completely crushed. Densification begins when the cell walls come in contact and is complete when the relative density reaches 1. The field boundary (green line) defining the onset of densification is determined by the arguments leading to the following equation[50].

$$\frac{\sigma}{E_s} = 0.19\frac{\sigma_y}{E_s}(1-\varepsilon)^{3/2}\{1-\left(\frac{1-\varepsilon}{3}\right)^{1/3}\} \qquad [2]$$

Overlaying the fields are stress-strain curves representing foams with initial relative densities ranging from 0.08 to 0.19. The diagram delineates the domains of behavior for three defor- mations across the range of densities. These curves exhibit a linear elastic phase followed by a plateau indicative of plastic collapse and lastly, densification regime. As illustrated in the diagram, the field boundary diverges from the onset of densification, with the empirical line (depicted as a dotted line) offering a more realistic depiction compared to the calculated boundary. This empirical line was established at approximately twice the compressive stress level. The discrepancy arises due to the utilization of Equation (2), which is intended for rigid plastic foam materials with significantly lower Young's modulus, despite the glass material having a Young's modulus of around 60 GPa. Consequently, this leads to lower normalized stress values, providing an explanation for the deviation observed in the densification field boundary.

4. TAILORABLE ENERGY ABSORPTION

Applications focused on crashworthiness, such as safety systems for occupants in vehicles or aircraft, stand to gain significant advantages from materials capable of adjustable energy absorption. This capability allows for a gradual increase in stroking load, thereby diminishing acceleration and peak stress levels encountered during impact. For example, lighter passengers in seats designed for heavier passengers may face stress beyond safety limits, while heavier occupants in seats designed for lighter individuals may experience excessive stress due to inadequate energy absorption. Such impacts often cause bodily harm, including damage to the intervertebral disc, leading to prolonged reductions in quality of life[51,52]. Passenger seats, with an energy absorber tailored for a specific occupant weight, can handle various weights efficiently.

Functionally graded foam utilizes a density gradient to enhance energy absorption at various stress levels. Research has shown that adjusting the density gradient can tailor the profiles and amplitudes of stress waves, thus improving energy absorption and reducing damage[41,53,54,55,56]. The mechanical response of a functionally graded foam sample can be tailored by changing the local density or selecting different cell materials. Typically, layers of varying densities are adhered together with glue to create a structure with graded density.

4.1 Layered Foam Structures

The DPP system, coupled with an optimized glass foam fabrication process, facilitates the creation of multilayered foam structures to fine-tune their stress vs. strain profile and energy absorption capability. The potential tailorability of glass foam by sequential compression of a bilayer structure is shown in figure 8. This data demonstrates that it is feasible to tailor compressive stress–strain curves within certain levels. This tailoring of the

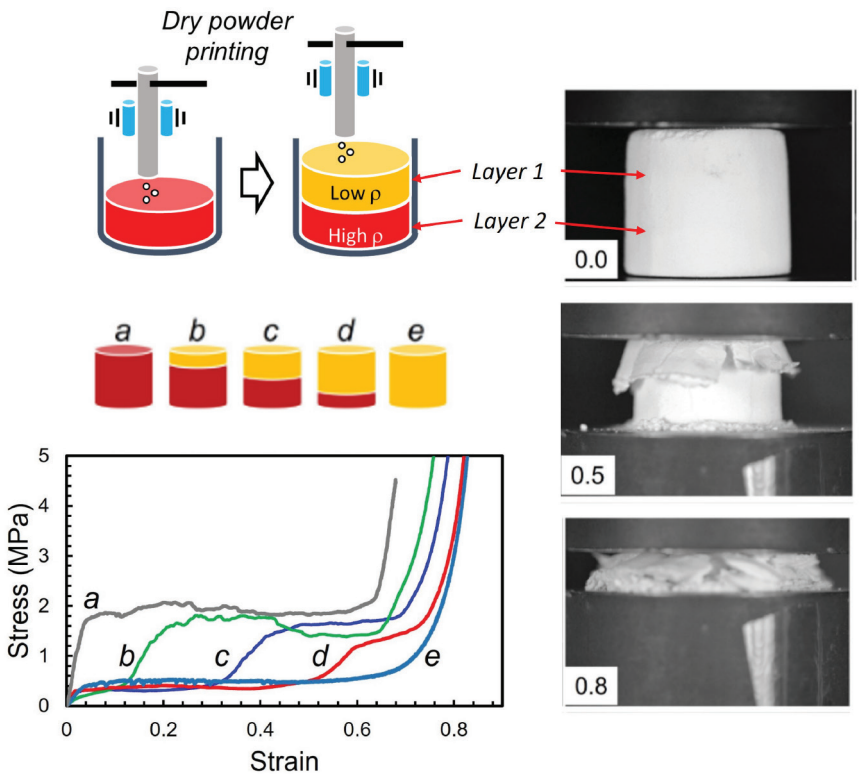

Figure 8. (Left) A schematic drawing of the DPP process alongside stress-strain curves for foam samples with varying ratios of layer thickness. (right) Images of compression testing of sintered bilayer foam. The numbers in the inset are strain.

energy absorption (the area under the stress-strain curve) was achieved for bilayer foam samples fabricated through sintering and subjected to quasi-static uniaxial compressive load.

The stress–strain profiles of bilayer foams with different thickness ratios of layer 1/layer 2, along with uniform foams of layer 1 and layer 2, are depicted in Figure 8. In this context, layer 1 represents low-density foam, while layer 2 represents high-density foam. Each bilayer foam curve displays a characteristic two-step stress–strain profile due to the sequential collapse of the two layers. The low-density layer 1 compresses first for all cases, reaching a plateau stress slightly below 0.5 MPa. This plateau stress persists during the plastic collapse of the microstructure of layer 1. The transition to the second plateau, marked by compression of the high-density layer 2, varies with the layer thickness ratio, with thinner layer 1 ending the first plateau earlier (curve (b)) compared to thicker layer 1 (curve (d)). The transition slope also changes with the thickness ratio, with curve (b) exhibiting a steeper transition and curve (d) the least steep. The onset of densification and the transition to the slope can be adjusted according to the thickness of the layer, offering potential injury reduction opportunities. Second plateau stress persists during the plastic collapse of the microstructure of layer 2. The images in Figure 8 illustrate the bilayer glass foam, with a specific focus on sample (c), during uniaxial compression testing. Compression of the bilayer foam began from its upper layer (layer 1), followed by significant spalling of the side walls in the lateral direction at a strain of 0.5. At a strain of 0.8, the bottom layer (layer 2) is fully compressed.

4.2 Deformation-Mechanism Map for Bilayers

The deformation map for the bilayer system is depicted in Figure 9. As compression initiates, all foams exhibit linear elastic deformation initially, followed by plastic collapse, culminating in the densification phase. These three distinct domains are delineated for all bilayer samples, represented by green lines. The boundary of the linear-elastic field is determined from Equation [1]. The boundary between plastic collapse and densification is determined from Equation [2]. The stress-strain curve of the bilayer foam displays a two-step profile, attributed to the sequential collapse of its layers. Consequently, an additional boundary can be incorporated for the second layer, positioning the boundaries of the bilayer samples between those of the two uniform foams. The equation mentioned above underwent modification to construct the map for the bilayer systems. Since the materials used in all foam samples are identical, a value of 0.01 was used for σ/E_s to delineate the boundaries. The equation was adjusted to accommodate the shift to the second peak stress. As illustrated in the figure, the red dotted lines represent boundaries for each bilayer foam, indicating the first plateau field attributed to the plastic collapse of the first layer, followed by the phase of the second linear elasticity of the bilayer system. The densification line in the figure also deviates from the onset of densification, and thus an empirical boundary is included on the diagram.

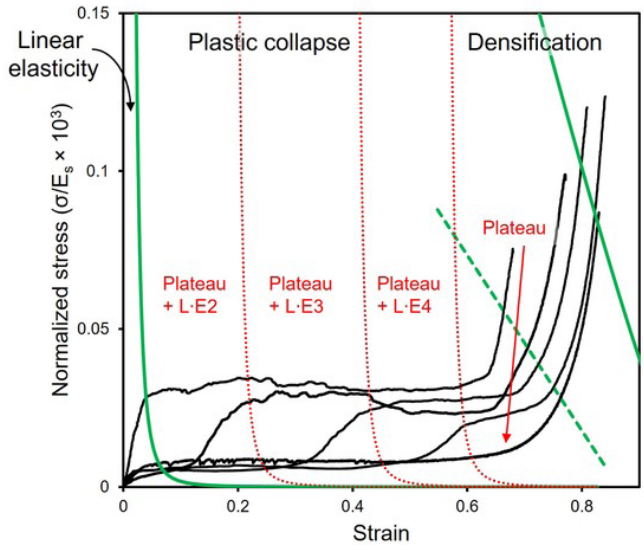

Figure 9. A deformation-mechanism map is developed for bilayer glass foams exhibiting various ratios of layer thickness. Each layer possesses relative densities of 0.08 and 0.17, respectively. In the map, a heavy green line delineates the field boundary, while dotted line indicates empirical boundaries.

4.3 Bilayer Interface

A key feature of bilayer structures is the interface, which experiences enhancements when utilizing the DPP system to achieve precise density control in the powder compact, and subsequent co-sintering process. Figure 10 depicts compression tests on epoxy-bonded samples, exhibiting a distinctly different behavior from their sintered counterparts. Three different density foams were configured to create bilayered structures. Layer 1 has the lowest density, layer 2 has a middle density, and layer 3 has the highest density. The tests were carried out on bilayer structures consisting of layer 1 and layer 3, as well as layer 2 and layer 3. The epoxy-bonded foam in Figure 10 (a) presents a 75% modulus increase for layer 1/layer 3, with stress-strain curves similar to sintered foams up to a strain of approximately 0.35. As the second layer (layer 3) undergoes compression, the stress peaks at 1.7 MPa for the sintered foam, but the epoxy-bonded foam exhibits a higher stress overshoot (2.3 MPa) compared to the sintered foam. This difference in stress transition could impact injury outcomes, with smoother transitions preferred. Densification starts around 0.68 strain for both types. In the layer 2/layer 3 system (Figure 10(b)), the epoxy-bonded foam does not display a two-step stress-strain profile; instead, it exhibits uniform compression behavior similar to uniform foams. The density contrast between layers significantly influences the compressive behavior. When the density difference between layer 2 and layer 3 is small, the bilayer structure behaves akin to a uniform sample. Conversely,

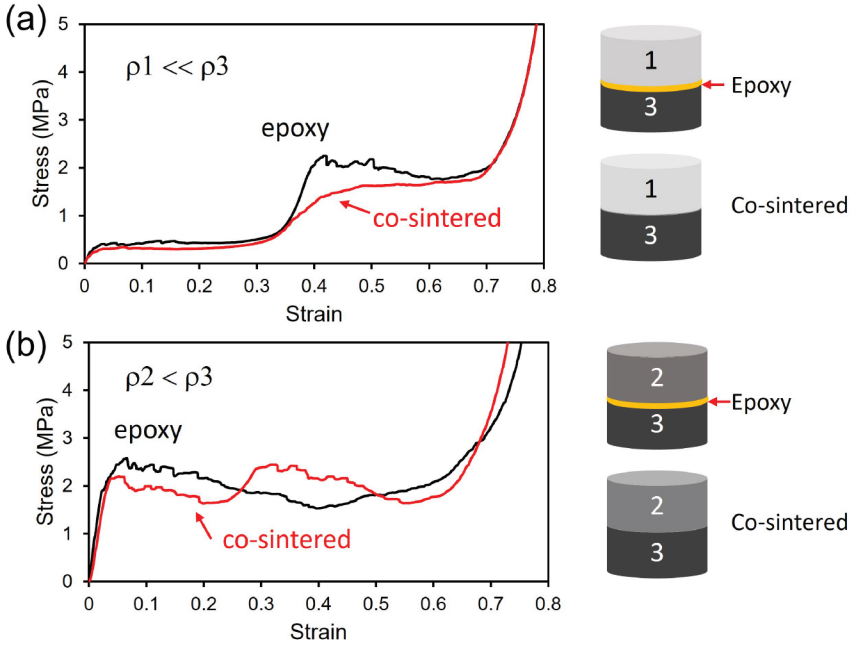

Figure 10. (a) Stress–strain curves of sintered bilayer foam of layer 1/layer 3 (red line), and epoxy-bonded bilayer foam (black line). (b) Stress–strain curves of sintered bilayer foam of layer 2/layer 3 (red line), and epoxy-bonded bilayer foam (black line).

the sintered foam still demonstrates a two-step stress-strain profile, thereby enabling tailorable energy absorption. Sintering bilayer foams produces glass foam samples with precise control of density. Even finer density control could be achieved by employing multiple layers in conjunction with dry powder printing, enabling further tailoring of the stress vs strain profile.

5. CONCLUSION

High-strength and low-density glass foams can be produced by sintering hollow glass microspheres. Crashworthiness, buoyancy, and load-bearing structural applications can benefit from glass foams. We demonstrated that both monolithic (single density) and functionally graded (layerwise density tailoring) glass foam can be fabricated using a dry powder printing (DPP) system, where the axial density profile can be precisely controlled by printing HGMs with different densities. The implementation of a sintered bilayer can reduce the stress induced under quasi-static crush as compared to glued bilayers, because of the improved consolidation and uniformity of the interface in sintered foams.

Implementing multilayer foam structures by increasing the number of layers, as well as the corresponding layerwise density, in future work, may enable finer tailorability of the stress-strain profile, and a smoother increase in stress to be achieved for a particular impact requirement.

ACKNOWLEDGMENTS

The research was jointly supported by the State of Maryland under a Maryland Technology Enterprise Institute (MTECH), Maryland Industrial Partnerships (MIPS) Contract Agreement #5819. The authors also thank Joseph Naft, Director of the Maryland Industrial Partnerships Program, for his encouragement and support. Additional support was provided Under a Phase 1 and Phase 2 SBIR contract from the US Navy.

REFERENCES

1. T.P. Hutchinson (2014). "Peak acceleration during impact with helmet materials: Effects of impactor mass and speed." *Euro. J. Sport Science* 14.sup1 S377–S382. https://doi.org/10.1080/17461391.2012.705334

2. N. Gupta, S.E. Zeltmann, V.C. Shunmugasamy, and D. Pinisetty (2014). "Applications of polymer matrix syntactic foams." *JOM*, 66:245–254. https://doi.org/10.1007/s11837-013-0796-8

3. G. Subhash, Q. Liu, and X. Gao. (2006). "Quasistatic and high strain rate uniaxial compressive response of polymeric structural foams." Inter. *J. Impact Engin*. 32:1113–1126. https://doi.org/10.1016/j.ijimpeng.2004.11.006

4. B.A. Gama, T.A. Bogetti, B.K. Fink, C. Yu, T.D. Claar, H.F. Eifert, J.W. Gillespie Jr. (2001). "Aluminum foam integral armor: a new dimension in armor design." *Composite Structures* 52(3-4):381–395. https://doi.org/10.1016/S0263-8223(01)00029-0

5. M. Garcia-Avila, M. Portanova, and A. Rabiei. "Ballistic performance of a composite metal foam-ceramic armor system." *Procedia Materials Science* 4:151–156. https://doi.org/10.1016/j.mspro.2014.07.571

6. C.W. Ong, C.W. Boey, R.S. Hixson, J.O. Sinibaldi (2011). "Advanced layered personnel armor." Inter. *J. Impact Engin.,* 38(5):369–383. https://doi.org/10.1016/j.ijimpeng.2010.12.003

7. E.J. Kuncir, R.W. Wirta, and F.L. Golbranson (1990). "Load-bearing characteristics of polyethylene foam: an examination of structural and compression properties." *J. Rehab. Res. Dev*., 27(3):229–238. https://doi.org/10.1682/jrrd.1990.07.0229

8. H. Chang, L. Zhang, W. Dou, and H. Zhang (2021). "Improved strategies for the load-bearing capacity of aluminum-PVC foam sandwich floors of a high-speed train". *J. Mech. Sci. Tech*. 35(2):651–659. https://doi.org/10.1007/s12206-021-0125-z

9. D.H. Kallas and C.K. Chatten (1969). "Buoyancy materials for deep submergence." *Ocean Engineering* 1(4):421–431. https://doi.org/10.1016/0029-8018(69)90014-6

10. L.W. Watkins (1982). "Syntactic foam buoyancy for ultradeep marine riser." *Offshore Technology Conf.* Houston, TX, May 3-6. https://doi.org/10.4043/4320-MS

11. C. Kim and J.-R. Youn (2000). "Environmentally friendly processing of polyurethane foam for thermal insulation." *Polymer-Plastics Technology and Engineering*, 39(1):163–185. https://doi.org/10.1081/PPT-100100022

12. Z. Ma et al. (2021). "Bioinspired, highly adhesive, nanostructured polymeric coatings for superhydrophobic fire-extinguishing thermal insulation foam." *ACS Nano* 15(7):11667–11680. https://doi.org/10.1021/acsnano.1c02254

13. W. Gu et al. (2020). "Multifunctional bulk hybrid foam for infrared stealth, thermal insulation, and microwave absorption." *ACS Applied Materials & Interfaces,* 12(25):28727–28737. https://doi.org/10.1021/acsami.0c09202

14. T.J. Lu, H.A. Stone, and M.F. Ashby (1988). "Heat transfer in open-cell metal foams." *Acta Materialia*, 46(10):3619–3635. https://doi.org/10.1016/S1359-6454(98)00031-7

15. T. Hung, J. Huang, Y. Wang, and K. Lin (2014). "Inorganic polymeric foam as a sound absorbing and insulating material." *Construction and Building Materials* 50:328–334. https://doi.org/10.1016/j.conbuildmat.2013.09.042

16. A. Cunningham and N.C. Hilyard (1994). "Physical behaviour of polymeric foams—An overview." *Low Density Cellular Plastics*, Springer, Dordrecht, Chapter 1.pp. 1–21. https://doi.org/10.1007/978-94-011-1256-7_1

17. K. Yang, J. Zou, and J. Shen (2020). "Vibration and noise reduction optimization design of mine chute with foam aluminum laminated structure." *Inter. J. Engin.* 33(8):1668–1676. https://doi.org/10.5829/ije.2020.33.08b.26

18. L.-P. Lefebvre, J. Banhart, and D.C. Dunand. (2008). "Porous metals and metallic foams: current status and recent developments." *Adv. Engin. Mater.*, 10(9):775–787. https://doi.org/10.1002/adem.200800241

19. L. Giani, G. Groppi, and E. Tronconi (2005). "Mass-transfer characterization of metallic foams as supports for structured catalysts." *Industrial & Engineering Chemistry Research*, 44(14):4993–5002. https://doi.org/10.1021/ie0490886

20. L.J. Gibson and M.F. Ashby (1997). *Cellular Solids,* Cambridge University Press, pp. i–vi.

21. M. Vural and G. Ravichandran (2003). "Dynamic response and energy dissipation characteristics of balsa wood: experiment and analysis." *Inter. J. Solids Struct.,* 40(9): 2147–2170. https://doi.org/10.1016/S0020-7683(03)00057-X

22. J.L. Yu, J.R. Li, and S.S. Hu (2006). "Strain-rate effect and micro-structural optimization of cellular metals." *Mechanics of Materials,* 38(1-2):160–170. https://doi.org/10.1016/j.mechmat.2005.05.018

23. R. Bouix, P. Viot, and J.-L. Lataillade (2009). "Polypropylene foam behaviour under dynamic loadings: Strain rate, density and microstructure effects." *Inter. J. Impact Engin*. 36(2):329–342.https://doi.org/10.1016/j.ijimpeng.2007.11.007

24. M. F. Ashby et al. (2000). *Metal Foams: A Design Guide*. Elsevier.

25. Wiest, C.A. MacDougall, and R.D. Conner (2014). "Optimization of cellular solids for energy absorption." *Scripta Materialia*, 84:7–10. https://doi.org/10.1016/j.scriptamat.2014.02.013

26. D. Ghosh, A. Wiest, and R.D. Conner (2016). "Uniaxial quasistatic and dynamic compressive response of foams made from hollow glass microspheres." *J. European Ceramic Society*, 36(3):781–789. https://doi.org/10.1016/j.jeurceramsoc.2015.10.018

27. C Swetha and R. Kumar (2011). "Quasi-static uni-axial compression behaviour of hollow glass microspheres/epoxy based syntactic foams." *Materials & Design*, 32(8-9):4152–4163. https://doi.org/10.1016/j.matdes.2011.04.058

28. H. Kim and H. Oh (2000). "Manufacturing and impact behavior of syntactic foam." *J. Appl. Polymer Sci.,* 76:1324–1328.https://doi.org/10.1002/(SICI)1097-4628(20000523)76:8<1324::AID-APP13>3.0.CO;2-%23M.

29. M. Ozkutlu, C. Dilek, and G. Bayram (2018). "Effects of hollow glass microsphere density and surface modification on the mechanical and thermal properties of poly (methyl methacrylate) syntactic foams." *Composite Struct.* 202:545– 550. https://doi.org/10.1016/j.compstruct.2018.02.088

30. J. Park, J. Howard, A. Edery, M. DeMay and N.M. Wereley (2021). "Bilayer glass foams with tunable energy absorption via localized void clusters." *Adv. Engin. Mater.,* 23(9):2100105. https://doi.org/10.1002/adem.202100105

31. J. Park, J. Howard, A. Edery, M. DeMay and N.M. Wereley (2019)."Process parameter effects on cellular structured materials using hollow glass spheres." *Mater. Manuf. Processes* 34(9):1026–1034. https://doi.org/10.1080/10426914.2019.1594256

32. A. Dasan et al. (2022). "3D Printing of Hierarchically Porous Lattice Structures Based on Akermanite Glass Microspheres and Reactive Silicone Binder." *MDPI J. Functional Biomaterials*, 13(1):8. ttps://doi.org/10.3390/jfb13010008

33. Z. Wang et al. (2022). "Preparation of lightweight glass microsphere/Al sandwich composites with high compressive properties." *Materials Letters*, 308:131220. https://doi.org/10.1016/j.matlet.2021.131220

34. A.V.Ryzhenkov et al. (2015). "Review of binding agents in syntactic foams for heat-insulating structures in power industry Facilities." *Modern Appl. Sci.*, 9(4):96. http://dx.doi.org/10.5539/mas.v9n4p96

35. E. Baumeister and S. Klaeger (2003). "Advanced new lightweight materials: hollow-sphere composites (HSCs) for mechanical engineering applications." *Adv. Engin. Mater.,* 5(9):673–677. https://doi.org/10.1002/adem.200320137

36. N. Gupta and D. Pinisetty (2013). "A review of thermal conductivity of polymer matrix syntactic foams—effect of hollow particle wall thickness and volume fraction." *JOM*, 65(2):234–245. https://doi.org/10.1007/s11837-012-0512-0

37. M. Soshkin (2016). "Autonomous Underwater Vehicle Manufacturing in the US". *IBIS- World Industry Report*, OD4429.

38. M. Soshkin (2016). "Body Armor Manufacturing in the US." *IBISWorld Industry Report*, OD5952.

39. I. Peters (2016). "Car & Automobile Manufacturing in the US." *IBISWorld Industry Report*, 33611a.

40. C. Negroni (2012). "Questioning Safety of Heavy Passengers on Planes." *The New York Times*, May 7.

41. I. Maskery, A. Hussey, and R. Hague, (2017). "An investigation into reinforced and functionally graded lattice structures." *J. Cellular Plastics*, 53(2):151–165. https://doi.org/10.1177/0021955X1663903

42. S.G. Mosanenzadeh, H.E. Naguib, C.B. Park, and N. Atalla (2015). "Design and development of novel bio-based functionally graded foams for enhanced acoustic capabilities." *J. Mater. Sci.* 50:1248–1256. https://doi.org/10.1007/s10853-014-8681-6

43. W. Van Grunsven et al. (2014) "Fabrication and mechanical characterisation of titanium lattices with graded porosity." *Metals* 4(3):401–409. https://doi.org/10.3390/met4030401

44. J. Park, J. Howard, A. Edery, M. DeMay, and N.M. Wereley (2022). "Tunable energy absorbing property of bilayer amorphous glass foam via dry powder printing." *MDPI Materials*, 15(24):9080. https://doi.org/10.3390/ma15249080

45. S. Yang and J.R.G. Evans (2007). "Metering and dispensing of powder; the quest for new solid freeforming techniques." *Powder Tech*. 178(1):56–72. https://doi.org/10.1016/j.powtec.2007.04.004

46. S. Yang and J.R.G. Evans (2004). "Acoustic control of powder dispensing in open tubes." *Powder Tech*. 139(1):55–60. https://doi.org/10.1016/j.powtec.2003.10.008

47. T. Stichel et al. (2014). "Powder layer preparation using vibration-controlled capillary steel nozzles for additive manufacturing." *Physics Procedia* 56:157–166. https://doi.org/10.1016/j.phpro.2014.08.158

48. X. Lu, S. Yang, and J.R.G. Evans (2007). "Dose uniformity of fine powders in ultrasonic microfeeding." *Powder Tech.,* 175(2):63–72. https://doi.org/10.1016/j.powtec.2007.01.029

49. J.B. Knight et al. (1995). "Density relaxation in a vibrated granular material." *Physical Review E*, 51(5):3957. https://doi.org/10.1103/PhysRevE.51.3957

50. M.F. Ashby and R.F. Mehl Medalist (1983). "The mechanical properties of cellular solids." *Metall. Trans. A,* 14:1755-1769. https://doi.org/10.1007/BF02645546

51. J.A. Pramudita et al. (2009). "Development of a head-neck finite element model and analysis of intervertebral strain response during rear impact." *Trans. Japan Soc. Mechanical Engin. Part A*, 75(759):1549–1555. https://doi.org/10.1299/kikaia.75.1549

52. K.H. Yang et al. (2006). "Development of numerical models for injury biomechanics research: a review of 50 years of publications in the Stapp Car Crash Conference." *Stapp Car Crash J*., 50:429-90. https://doi.org/10.4271/2006-22-0017

53. A.H. Brothers and D.C. Dunand (2008). "Mechanical properties of a density-graded replicated aluminum foam." In: *Mater. Sci. and Eng., A* 489(1-2): 439–443. https://doi.org/10.1016/j.msea.2007.11.076

54. H. Lin, L. Lv, J. Zhang and Z. Wang (2019). "Energy-absorbing performance of graded Voronoi foams." *J. Cellular Plastics* 55(6):589–613. https://doi.org/10.1177/0021955X198534

55. A. Ajdari, S. Babaee, and A. Vaziri (2011). "Mechanical properties and energy absorption of heterogeneous and functionally graded cellular structures." *Procedia Engineering* 10:219–223. https://doi.org/10.1016/j.proeng.2011.04.039

56. S. Kiernan, L. Cui, and M.D. Gilchrist (2009). "Propagation of a stress wave through a virtual functionally graded foam." *Inter. J. Non-Linear Mech*. 44(5):456–468. https://doi.org/10.1016/j.ijnonlinmec.2009.02.006